INORGANIC CHEMISTRY
FRONTIERS

RESEARCH ARTICLE

View Article Online
View Journal | View Issue

Cite this: *Inorg. Chem. Front.*, 2021, **8**, 405

The complete catalytic mechanism of xanthine oxidase: a computational study†

Pedro M. G. Ribeiro,‡[a] Henrique S. Fernandes, ‡[a] Luísa B. Maia, [b] Sérgio F. Sousa, [a] José J. G. Moura [b] and Nuno M. F. S. A. Cerqueira *[a]

In this article, quantum mechanical/molecular mechanical (QM/MM) methods were used to study the full catalytic mechanism of xanthine oxidase (XO). XO catalyzes the conversion of xanthine (XAN) to uric acid (URC), in the presence of a molybdenum cofactor (Moco). The mechanism occurs through four reaction steps. Initially, the proton from the hydroxyl group of Moco passes to Glu1261 and the activated hydroxyl group makes a nucleophilic attack on XAN. Then, a hydride is transferred from the tetrahedral intermediate to the sulfur atom of the Moco, reducing Mo(VI) to Mo(IV). In the third step, one molecule of URC is formed through its protonation by Arg880. Once this reaction is complete, FAD is reduced to $FADH_2$, oxidizing Mo (IV) to its initial oxidation state of Mo(VI). The enzymatic turnover is achieved with the reaction of one water molecule with the Moco. The rate-limiting step of the full catalytic mechanism is the hydride transfer that requires a free activation barrier of 16.9 kcal mol^{-1}, which closely agrees with the experimental k_{cat} value (18.3 s^{-1}), which corresponds to approximately 15.7 kcal mol^{-1}. This work also elucidates the key role played by Arg880 in the catalytic mechanism and the importance of Glu802 in the binding of the substrate. Both residues were previously shown to be important by mutagenesis studies, but their role was still not clearly understood. Additionally, it was observed that the presence of a tunnel of water molecules located close to Moco and Glu1261 is important for the enzymatic turnover. The determined transition state structures can now be used to help the development of transition-state analog inhibitors targeting XO.

Received 25th August 2020,
Accepted 30th October 2020

DOI: 10.1039/d0qi01029d

rsc.li/frontiers-inorganic

Introduction

Xanthine oxidase (XO), E.C. 1.17.3.2, is a Mo-dependent enzyme involved in the catalysis of the two rate-limiting steps in the degradation of purine nucleotides. XO catalyzes the oxidation of hypoxanthine (HPA) into xanthine (XAN) and XAN into uric acid (URC). The full process requires two water molecules and two dioxygen molecules that are converted into two hydrogen peroxide molecules[1] (Fig. 1). Structurally, XO is a homodimer enzyme-containing 1333 amino acid residues per subunit.

XO has been extensively studied throughout the years due to the relationship of this enzyme with some diseases such as gout, the formation of uric acid stones, and xanthinuria. Gout and uric acid stone formation (hyperuricemia)[2–7] are caused by intense activity of XO that increases the levels of URC. Consequently, uric acid tends to precipitate in joints, skin, and blood capillaries in the form of needle-like crystals causing pain.[7] URC can also originate kidney stones in the form of sodium urate crystals. Xanthinuria is a rare genetic disorder that is associated with low XO activity and that can lead to high levels of circulating XAN and is responsible for some disease conditions such as renal failure.[8,9]

The main research is devoted to the search for inhibitors of XO that could be used to treat diseases such as gout. Actually, there are already a few commercial inhibitors used in the clinic: *e.g.* allopurinol[10,11] and 6-mercaptopurine.[12] However, the search for better new inhibitors continues,[13–21] largely because of the increase in gout incidence[6,7] which reached almost 6 million cases in 2013.[22]

A lot of information regarding the catalytic mechanism of XO has been obtained through the years. Kinetic parameters of XO were determined experimentally, revealing a reaction rate of 30.0 s^{-1} for the conversion of HPA into XAN, and 18.3 s^{-1} for the oxidation of XAN into URC (pH 8.5 and 25 °C).[23] In terms of mutagenesis studies, Yamaguchi and collaborators[23] addressed the impact of the mutation of two residues at the active site of XO: Glu802 and Arg880 residues. The Glu802Val mutant showed a k_{cat} reduction to 1.35 s^{-1}, while the

[a]*UCIBIO@REQUIMTE, BioSIM, Departamento de Biomedicina, Faculdade de Medicina da Universidade do Porto, Alameda Professor Hernâni Monteiro, 4200-319 Porto, Portugal. E-mail: nunoscerqueira@med.up.pt*
[b]*LAQV, REQUIMTE, NOVA School of Science and Technology, Campus de Caparica, 2829-516 Caparica, Portugal*

†Electronic supplementary information (ESI) available. See DOI: 10.1039/d0qi01029d

‡Both authors have equally contributed to the calculations presented in this article.

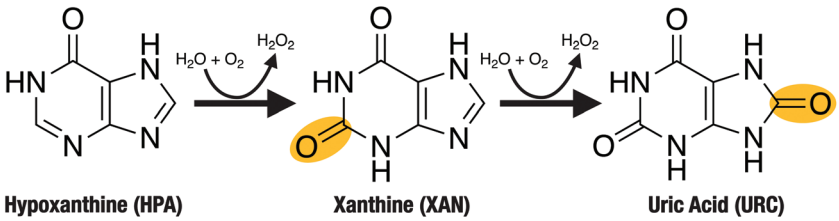

Fig. 1 Reactions catalyzed by XO: (1) oxidation of HPA to XAN and (2) oxidation of XAN to URC.

Arg880Met completely inactivates the enzyme. In spite of this knowledge, the specific steps involved in the catalytic mechanism are still poorly understood. Currently, there are two main proposals: one suggested by Yamaguchi and co-workers,[23] based on the kinetic data from mutations and X-ray structures; and a second one based on the QM and QM/MM work of Metz and Thiel[24,25] (Fig. 2).

Although Yamaguchi's proposal provides a simple explanation about how the mechanism occurs, it does not provide insights about the importance of a crystallographic water molecule placed between Glu1261 and Arg880. Moreover, the mechanism does not explain the importance of Arg880 since its mutation completely inactivates the enzyme.

In the proposal of Metz and Thiel, there is no explanation for the release of the product (URC), and the role of Arg880 is not completely clarified.

Those are the main pitfalls of the previously available mechanism proposals that were considered in this work which aims to provide, for the first time, a complete and atomistic detailed description of the catalytic mechanism of XO.

Methodology

Structure preparation

Among the structures of XO available in the Protein Data Bank (PDB), the structure deposited under the code 3AMZ[26] was used in this study. Although this structure is for bovine XO, the structure was solved with a good resolution (2.1 Å) and is the only XO structure co-crystallized with the product of the reaction in the active site. In fact, the existing structures of the human XO have worse resolution (2.6 Å (ref. 27) and 3.59 Å (ref. 28)) and do not include the substrate, product or analogues. Moreover, the sequence of the bovine form of XO has a similar identity of 89.65% when compared with the human form (BLAST).[29,30] In particular, the structure of both active sites is perfectly superimposable (Fig. S1†). The gaps present in the PDB structure 3AMZ, 166–191, 520–537, and 1321–1325, were filled by homology modeling (SWISS-model software).[31–34] The homology modeling was only used to fill the gaps in the PDB structure, accounting only about 4% of the entire protein sequence. Additionally, these gaps correspond to flexible loops in the enzyme's surface and are considerably far from the active site (Fig. S2†).

The final structure contains the entire homodimer, where each subunit includes two [2Fe–2S] clusters, a flavin adenine nucleotide (FAD) molecule, a molybdopterin cofactor (Moco), and a substrate (XAN) molecule.

Molecular dynamics simulation

A 22 ns molecular dynamics (MD) simulation was conducted to equilibrate the system and to provide a sample for choosing the initial structure for studying the catalytic mechanism. All the energy minimizations and MD simulations were conducted using GAFF[35] and ff99SB[36] force fields. The molecular mechanics (MM) parameters for Moco were obtained from the pub-

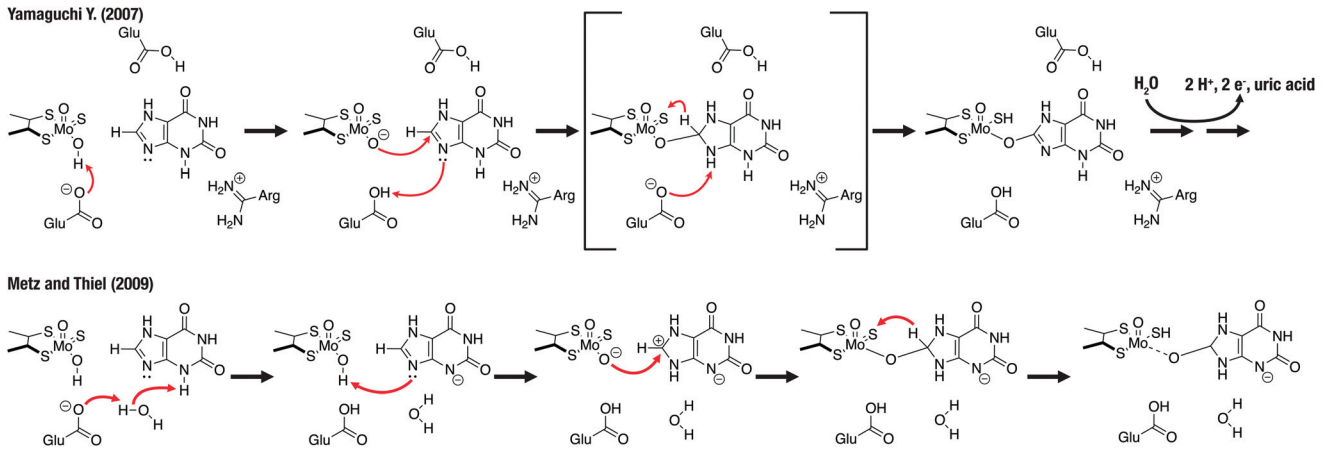

Fig. 2 Proposals of Yamaguchi Y. (2007)[23] and Metz and Thiel (2009)[24,25] for the catalytic mechanism of XO.

lication by Ferreira P. and co-workers,[37] whereas the parameters for [2Fe–2S], FAD, and XAN molecules were obtained through geometry optimization (HF/6-31G(d)) for charge determination and atomic topology assignment by antechamber software from the AMBER12 package.[38] The protonation of all amino acid residues of the protein was assessed using PROPKA[39,40] software.

Four sequential minimization steps were performed: (1) minimization of water molecules, (2) hydrogens, (3) all atoms except the backbone, and finally (4) the entire system. The MD simulation was performed using PMEMD software from the AMBER12 package,[38] a solvation box of TIP3P[41] type of water molecules, cutting-off non-bond interactions at 10.0 Å, and an integration time-step of 1 fs at the temperature of 310.15 K and pressure of 1.0 bar using the Langevin thermostat[42] and Berendsen barostat.[43]

QM/MM calculations

The initial structure for the QM/MM calculations was retrieved as a representative structure of the most populated cluster from the MD simulation.[44] The model was built using the molUP[45] plugin for Visual Molecular Dynamics (VMD)[46] software. The QM/MM model includes the full protein, the substrate (XAN), the Moco, and a 4.0 Å coating of water molecules around the full protein. The coating of water molecules mimics the solvent effect (water) around the enzyme, through intermolecular interactions and limiting the free movements of the solvent-exposed parts of the enzyme. The total system is composed of about 24 500 atoms that were treated using two different theoretical methods following a 2-layer subtractive ONIOM QM/MM approach.[47–49] The high-level (HL) layer included the Moco, a water molecule (two in the last step), the XAN molecule (except for the last step), and the Ala1043, Ser1044, Arg844, Glu1225, Glu766, and Gln731 amino acid residues, accounting for 84 to 97 atoms (Fig. S3†). The remaining atoms of the system were included in the low-level layer.

The geometry optimization of the HL layer was performed using the B3LYP[50] functional (DFT), based on the very good results in the study of biological systems. The 6-31G(d)[51–55] basis set and LanL2dz[56] pseudo-potential (Mo atom) were employed for the geometry optimizations as available in Gaussian 09.[57] During the catalytic mechanism, the oxidation state of the Mo atom changes from +6 to +4, and back to +6 during the enzymatic turnover. Accordingly, the spin multiplicity was set to 1 for all the calculations described in this manuscript.

The zero-point energy (ZPE) and thermal and entropic energy corrections were estimated at 310.15 K and 1.0 bar during the frequency calculations of TS and related minima structures. The activation and reaction Gibbs free energies, for each step, were calculated through the difference between the computed Gibbs free energies of TS or the product and the reactant, respectively.

The final energies were refined through single-point energy calculations using a more complete basis set: 6-311++G (3df,3pd).[54,58–62]

All the calculations were accomplished using Gaussian 09 software,[57] whereas the preparation of input files and analysis of results were made using the molUP[45,63] plugin for VMD.[46]

This general protocol has been used with success in the study of the catalytic mechanism of several different enzymes,[64–73] including other important Mo-dependent systems.[24,25,74–78]

The structures (PDB files) for the reactant, TS, and the product of each step as well as a detailed description of the QM/MM methodology are available in the ESI.†

Results and discussion

Based on the calculations performed and in comparison with the available experimental data, it can be concluded that the catalytic mechanism of XO occurs in four steps involving the oxidation of XAN (Fig. 3) to URC and a subsequent enzymatic turnover. During the two initial steps, a XAN molecule is oxidized to an anionic form of URC (URT). In the third step, URT is protonated before being released as URC. Finally, the Moco (Fig. 3) is oxidized, and a water molecule becomes coordinated to Mo, closing the catalytic cycle, and making XO ready to catalyze a new cycle.

Oxidation of XAN

The oxidation of XAN to URT is the main stage of the entire catalytic mechanism, and it happens in two sequential steps.

In the first step, Glu1261 abstracts the proton (HR) from the hydroxyl group that is coordinated to the Mo(VI) ion (R: 1.88 Å to P: 1.00 Å in the optimized minima), enhancing the nucleophilic character of the OR oxygen atom. Simultaneously, the OR oxygen makes a nucleophilic attack on carbon C11 of the XAN molecule (R: 2.59 Å; P: 1.46 Å). The negative charge, which is transferred to the XAN molecule, is stabilized by resonance through the conjugated π-system involving C11, N8, C7, C6, C3, and N4 atoms (Fig. 4). The charge transfer from Glu1261 to XAN is corroborated by the analysis of the electrostatic potential surfaces represented in Fig. 5.

In this step, Glu802 plays a key role in the stabilization of the negative charge that is generated in the transition state structure. The strengthening of this interaction is supported by the decrease of the hydrogen bond distance from 2.31 Å to 1.86 Å in the optimized structures.

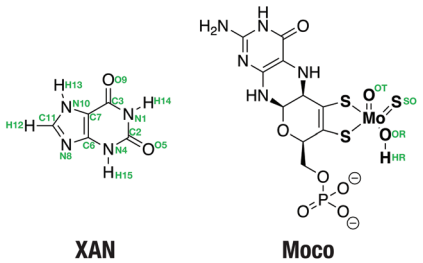

Fig. 3 Wedge-dash representation of XAN and Moco molecules.

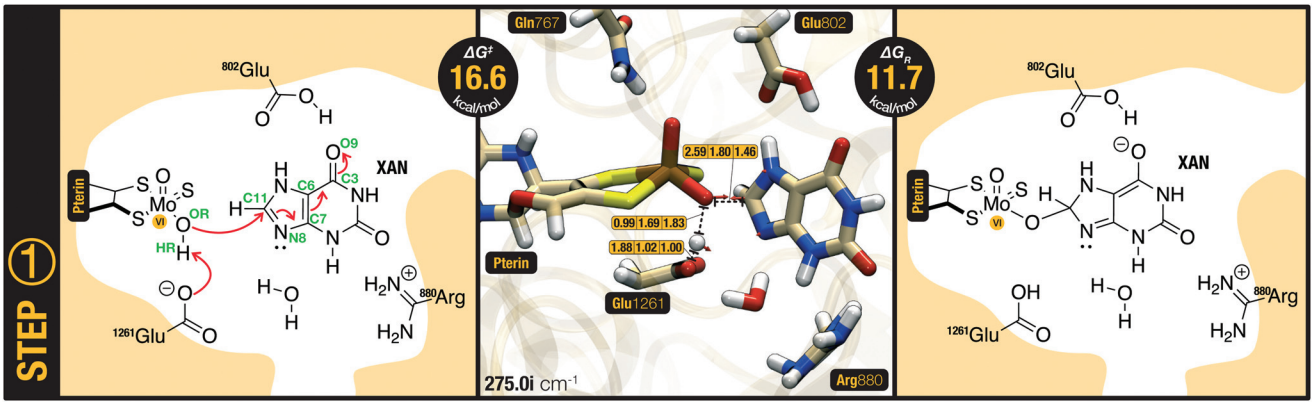

Fig. 4 Tridimensional representation of the active site residues, Moco, and XAN molecule at the active site of XO in the TS of step 1. The red arrows represent the vectors assigned to the atoms' vibrations associated with the imaginary frequency of the TS structure. Relevant interatomic distances for the reactant, TS, and product are labeled. Wedge-dash representation of the reaction and product of the reaction. The activation and reaction Gibbs free energies for this step, and the imaginary frequency assigned to the TS are shown.

The important role played by Glu802 goes in line with the experimental results obtained by Yamaguchi and co-workers,[23] since the Glu802Val mutation decreases the kinetics of the reaction (k_{cat} (WT) = 18.3 s^{-1} *vs.* k_{cat} (Glu802Val) = 1.35 s^{-1}). Glu802 not only seems to be important to position the XAN molecule in the active site, but also to stabilize the intermediate generated after the first step.

The TS of this reaction was confirmed by a single imaginary frequency at 275.0i cm^{-1}. This reaction requires an activation Gibbs free energy of 16.6 kcal mol^{-1} and is endergonic at 11.7 kcal mol^{-1}.

The second step of the oxidation of XAN involves the hydride transfer (H12) from carbon C11 to sulfur SO (R: 2.25 Å; P: 1.35 Å). The results suggest that this reaction is favored by the covalent bond established between oxygen OR and carbon C11 that decreases the distance between the hydrogen H12 to the sulfur SO that is coordinated to Moco. Consequently, the H12 hydride transfer is favored by the spatial proximity of the intermediate and the Moco, and the high electron density of the product of step 1, as represented in Fig. 5.

Although the overall reaction involves the transfer of two electrons and one proton (hydride) from XAN to Moco, this process can occur through three different mechanisms: a hydride transfer, a hydrogen–one electron-coupled transfer, or a proton–two electron-coupled transfer.

The hydride transfer is the simplest case where H12 and the two electrons are passed directly to sulfur SO. In this process, it is expected that H12 assumes a negative charge in the TS.

The hydrogen–one electron-coupled transfer occurs when H12 and one electron are passed to sulfur SO, and the second electron is transferred through the oxo-bridge established between Moco and XAN (Mo-OR-C11). In this case, the hydrogen H12 would assume a neutral charge during the TS.

Finally, the proton–two electron-coupled transfer involved the transfer of a proton (H12) directly to sulfur SO, and the two electrons are transferred to Moco *via* the oxo-bridge between Moco and XAN.

According to our calculations, the transference should follow a hydrogen–one electron-coupled mechanism, since the H12 hydrogen assumes an almost neutral atomic charge (Merz–Singh–Kollman) during the TS (charge: −0.019 a.u.).

During this second step, the Mo ion is reduced from oxidation number Mo(VI) to Mo(IV), triggering the cleavage of the bond between the Mo ion and oxygen OR (R: 2.00 Å; P: 2.20 Å) and consequent release of URT to the active site (Fig. 6).

This second step is considerable faster than step 1, accounting for an activation Gibbs free energy of 5.2 kcal mol^{-1}, and it is also a thermodynamically more favorable reaction (ΔG_R = −20.1 kcal mol^{-1}). The energies involved in this step makes the reverse reaction not possible under physiological conditions (due to the high activation energies for the reverse reaction), ensuring the continuity of the catalytic process.

The TS of this reaction is characterized by one imaginary frequency, at 1028.7i cm^{-1}, corresponding to the vibration of the atoms involved in the reaction.

The results demonstrate that after this reaction, URT is no longer bonded to the Mo ion, but remains in the active site waiting for its protonation on the N8 atom.

During this second step, the electron density that was lodged at XAN in the first step is now transferred to the Moco, where it is deeply stabilized (as can be seen in Fig. 5), contributing to an extremely favorable reaction.

Protonation of URT

The protonation of URT precedes the release of the product (URC) from the active site. For this step, two hypotheses were possible and were evaluated in this study: (1) protonation by the Arg880 residue and (2) protonation by the Glu1261 residue, both mediated by the same water molecule (Fig. 7).

According to the computed energies for the two hypotheses, the protonation of URT can be accomplished by Arg880 or Glu1261 residues. The activation free energies for the protona-

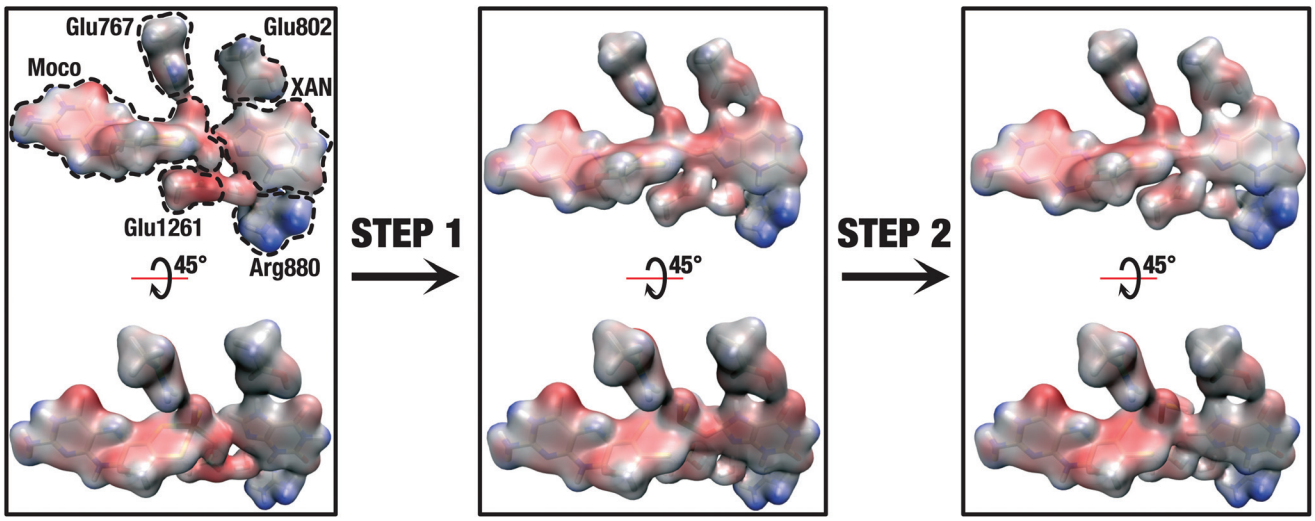

Fig. 5 Electrostatic potential mapped in the surface of the molecules involved in the reaction of steps 1 and 2.

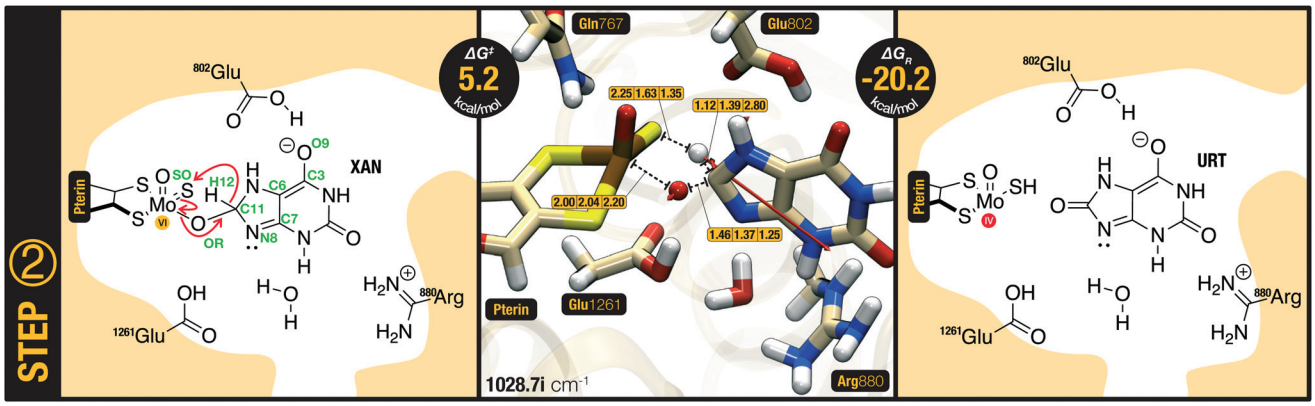

Fig. 6 Tridimensional representation of the active site residues, Moco, and XAN molecule at the active site of XO in the TS of step 2. The red arrows represent the vectors assigned to the atoms' vibrations associated with the imaginary frequency of the TS structure. Relevant interatomic distances for the reactant, TS, and product are labeled. Wedge-dash representation of the reaction and product of the reaction. The activation and reaction Gibbs free energies for this step, and the imaginary frequency assigned to the TS are shown.

tion by Arg880 and Glu1261 are 4.6 kcal mol^{-1} and 1.8 kcal, respectively. The main difference between both reactions is that the protonation promoted by Arg880 originates a more stable product (ΔG_R = −26.6 kcal mol^{-1}) when compared with the protonation mediated by Glu1261 (ΔG_R = +2.6 kcal mol^{-1}). In sum, one of the hypotheses (Glu1261) is kinetically more favorable, whereas the other one (Arg880) is thermodynamically more advantageous. However, we also observed that the product of the protonation by Glu1261 can be easily converted into the product of Arg880-mediated protonation. Consequently, the reaction where URT is protonated by Glu1261 can reach the same final product after a subsequent proton transfer from Glu1261 to Arg880.

Although both hypotheses are possible and interconvertible, it is more likely that XO follows the shortest and thermodynamically more favorable process, in which Arg880 is involved in the protonation of the URC molecule.

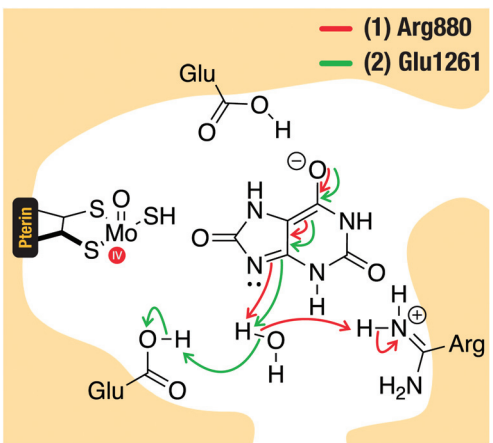

Fig. 7 Representation of the two hypotheses for the catalytic mechanism of step 3. (Red) Protonation of the URC molecule by the (red) Arg880 residue or (green) Glu1261 residue.

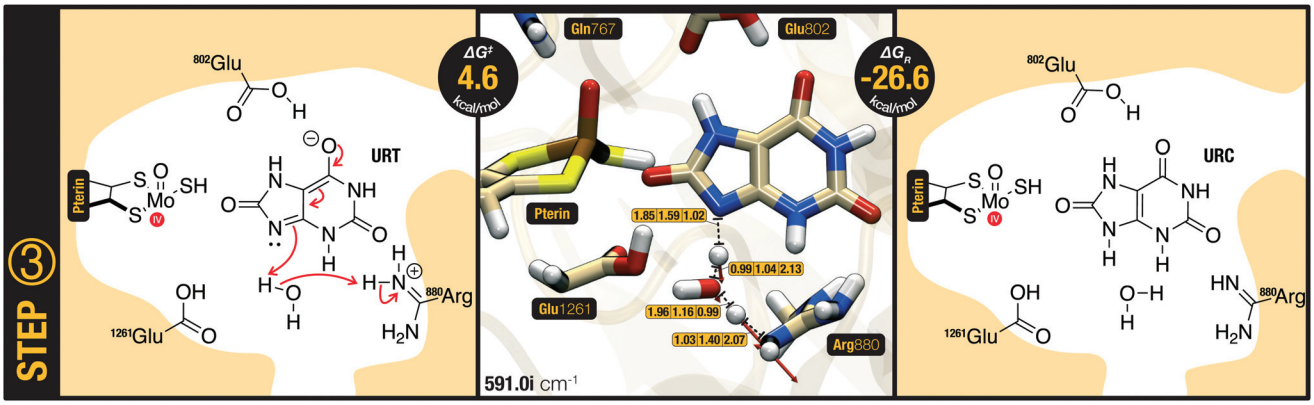

Fig. 8 Tridimensional representation of the active site residues, Moco, and URC molecule at the active site of XO in the TS of step 3. The red arrows represent the vectors assigned to the atoms' vibrations associated with the imaginary frequency of the TS structure. Relevant interatomic distances for the reactant, TS, and product are labeled. Wedge-dash representation of the reaction and product of the reaction. The activation and reaction Gibbs free energies for this step, and the imaginary frequency assigned to the TS are shown.

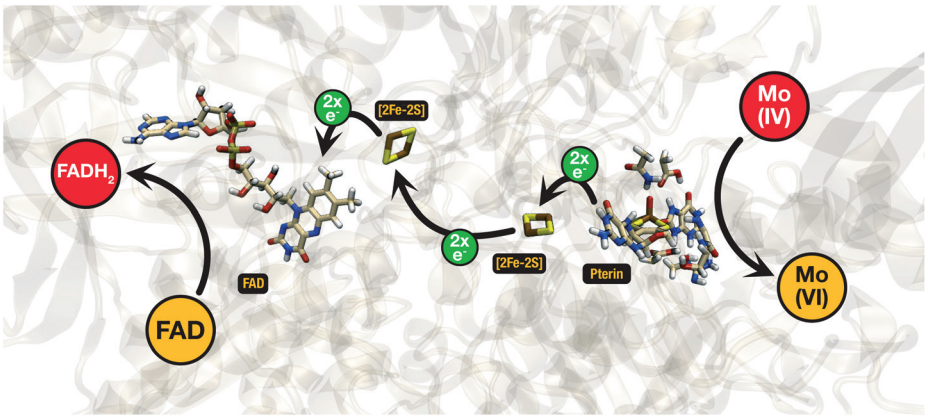

Fig. 9 Tridimensional representation of the active site residues, the two [2Fe–2S] clusters, and the FAD cofactor. Scheme of the oxidation of the Mo ion, the consequent flow of electrons through the [2Fe–2S] clusters, and reduction of the FAD cofactor into $FADH_2$.

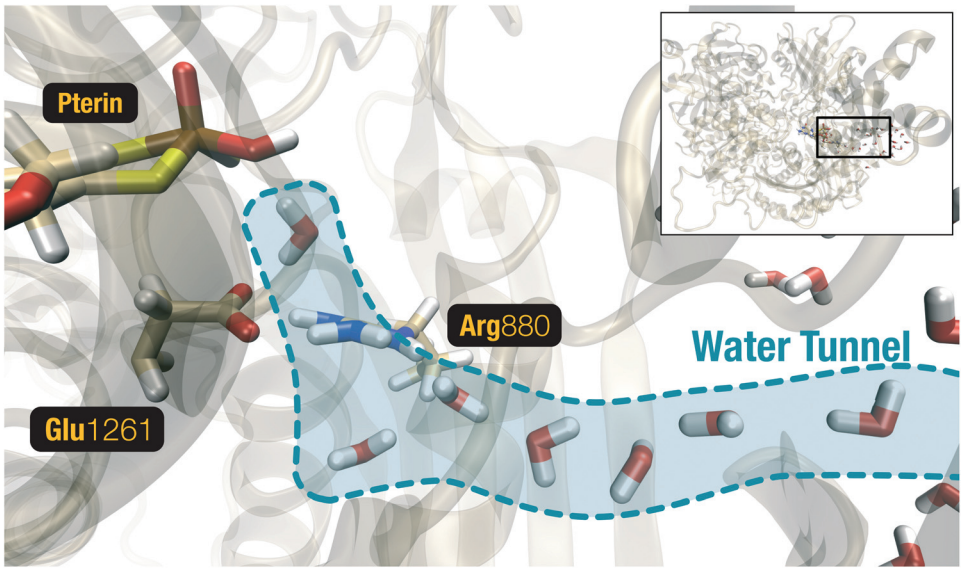

Fig. 10 Tridimensional representation of Moco, Glu1261, Arg880, and the water molecules filling the protein tunnel from the solvent to the bottom region of the active site obtained from the MD simulations.

In fact, this process, which involves a proton transfer from Arg880 to nitrogen N8 of URT mediated by a water molecule (as shown in Fig. 8), is very exergonic (ΔG_R = −26.6 kcal mol^{-1}), contributing (together with step 2) to the irreversibility of the XAN oxidation to URC. At this stage, URC becomes ready to be released from the active site as the final product of the reaction.

The simulations performed for this step provide an explanation for the importance of Arg880 for the mechanism, as suggested by the mutagenesis studies in which the Arg880Met mutation inactivates the enzyme.[23] The results of the present work show that Arg880 is the critical residue involved in the final protonation of URC and its release from the active site.

Enzymatic turnover

According to the calculations performed, at the end of step 3, URC is completely formed and is released from the active site of the enzyme.

At this moment, based on experimental evidence, the Mo ion is oxidized from Mo(IV) to Mo(VI). The two resulting electrons are transferred over ~24 Å through two [2Fe–2S] clusters until they reach the FAD cofactor. FAD acts as an electron acceptor species, being reduced to $FADH_2$ [79,80] (Fig. 9).

Once the URC molecule is generated, the next step of the catalytic mechanism involves the oxidation of the cofactor and reaction of Moco with one water molecule. This can happen in several ways: (i) the water molecule binds to Mo(IV) and only afterwards occurs the oxidation process (Mo(IV) to Mo(VI)); (ii) first occurs the reduction of the cofactor from Mo(IV) to Mo(VI) and only after, the reaction with the water molecule takes place; or (iii) the reduction of the cofactor occurs in a stepwise manner and involves the formation of transient Mo(V) species, which react with the water molecule.

Our calculations have shown that the water molecule can only coordinate with the Mo cofactor with Mo(VI) species. The same reaction cannot occur with the Mo(IV) or Mo(V) species. This goes in line with the theoretical results obtained in a recent study involving hAOX, which has the same cofactor and a similar active site.[81]

Once the Moco is oxidized again to Mo(VI), a water molecule can diffuse to the Moco's proximity, and bind to the Mo ion. To assess this hypothesis, the movement of the water molecules in the MD simulations was analyzed. The MD simulations performed in this work show that this water molecule can be supplied by a water tunnel located between Arg880 and Glu1261 residues (Fig. 10). The tunnel is approximately 18 Å in length and allows water molecules to flow inside the active site. Consequently, water molecules can occupy the active site simultaneously with the release of the URC molecules.

Once the water molecule fills the active site of XO, there are two possibilities for its reaction with the Mo ion: (i) the water molecule binds directly to the Mo ion with Glu1261 protonated or (ii) Glu1261 is deprotonated first and only afterwards one water molecule binds to the Mo ion. It is worth mentioning that nothing is known regarding how the proton is removed from Glu1261, but it is believed to involve the water molecules present on the XO active site once URC leaves the active site.

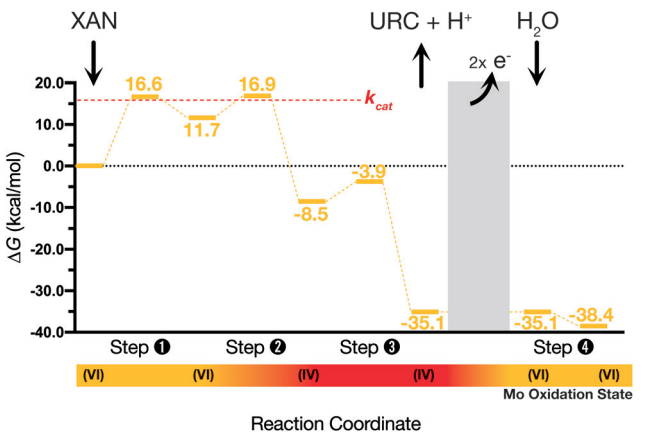

Fig. 12 Complete energy profile (B3LYP/6-311++G(3df,3pd),LanL2DZ:ff99SB) for the catalysis of the oxidation of XAN into URC by XO.

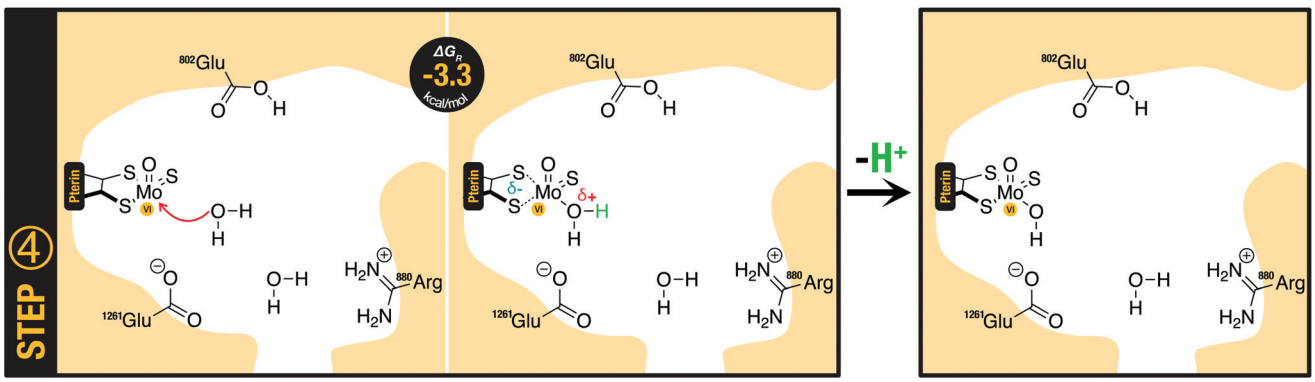

Fig. 11 Wedge-dash representation of the reaction and product of step 4, and the consequent deprotonation of the water molecule closing the enzymatic cycle. The reaction Gibbs free energy for this step is shown.

The two hypotheses were explored. The calculated free energies show that the first scenario is less favored from the kinetic and thermodynamic point of view ($\Delta G^{\ddagger}$ = 17.6 kcal mol^{-1}; ΔG_R = 15.2 kcal mol^{-1}) when compared with the second scenario in which the reaction is spontaneous (ΔG_R = −3.3 kcal mol^{-1}). At the end of this reaction, the water molecule becomes coordinated to the Mo ion (2.20 Å) and stabilized by one hydrogen bond provided by Glu1261 (1.50 Å) (Fig. 11).

The formation of this interaction justifies the more favorable nature of the reaction when Glu1261 is deprotonated. The transient positive charge developed on the water molecule is compensated (−0.04 a.u. *versus* 0.09 a.u. in the products) with the increase of the negative charge on the Moco cofactor. Consequently, both pterin's sulfur atoms become more distant from the Mo ion ([pterin]S–Mo R: 2.35 Å and 2.34 Å; P: 2.43 Å and 2.43 Å) (Fig. 11).

The results demonstrate that Glu1261 needs to lose its proton first in order to promote a spontaneous binding of the water molecule to the Mo ion. Afterward, the bonded water molecule loses one of its protons to a water molecule of the active site, completing the enzymatic turnover (Fig. 11).

Energy profile

The complete energy profile (Fig. 12) obtained for the mechanism of XO shows two initial energy-demanding steps, where the oxo group is transferred to the XAN molecule, followed by the hydride transfer that makes the reverse reaction

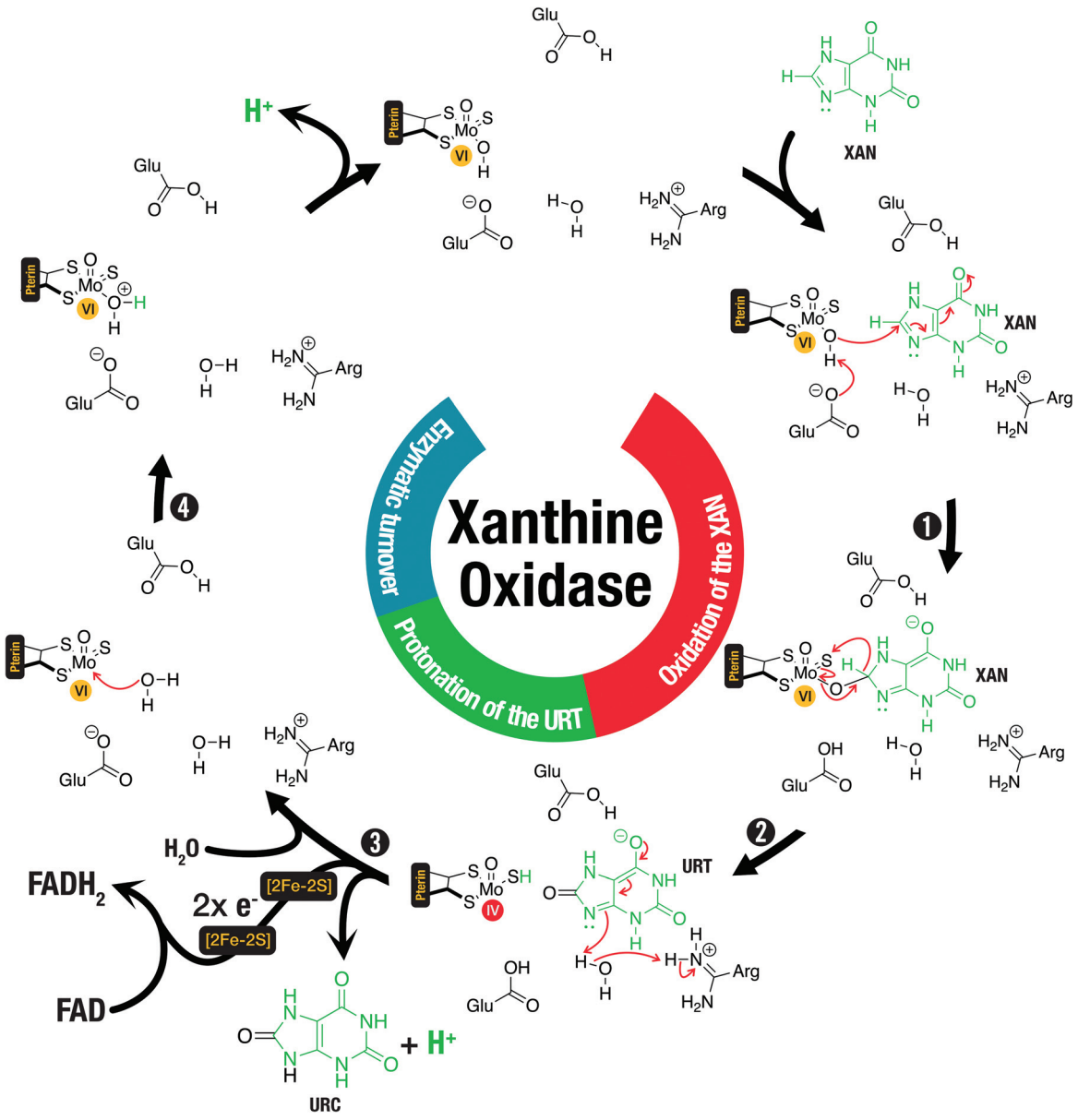

Fig. 13 Overview of the catalytic mechanism of the XAN oxidation into URC by XO.

impossible. The hydride transfer results in a very stable product (ΔG_R = −20.2 kcal mol^{-1}) that makes the reverse reaction impossible to occur under biological conditions. Furthermore, the subsequent step is even more exergonic, agreeing with the fact that this reaction should be irreversible. This idea is supported by the fact that, under biological conditions, high concentrations of URC are accumulated and are not converted again in XAN. The high stabilization of URC in the enzyme and the impairment of the reverse reaction explain how it was possible to obtain the crystallographic structure of such an intermediate using a reduced form of the XO.[26] This stabilization allows URC to stay in the active site of XO for enough time, preventing the reaction with water, and allowing its isolation, which is determined by X-ray crystallography.

In the last step, a water molecule coordinates with the Mo ion closing the catalytic cycle.

The two steps involved in the oxidation of the XAN molecule are the rate-limiting steps of the entire mechanism. The barrier of 16.9 kcal mol^{-1} of step 2 closely agrees with the predicted value (15.7 kcal mol^{-1}) based on the available kinetic parameters.[23]

Conclusions

In this work, the catalytic mechanism of the oxidation of XAN to URC by XO was studied using a computational ONIOM QM/MM approach.

The results provide, for the first time, a detailed and complete description of the entire catalytic mechanism of XO, completing previous works from Yamaguchi Y.,[23] and Metz and Thiel.[24,25] Moreover, it was possible to rationalize the role of Arg880 and Glu802 that have been previously shown to be important by mutagenesis studies.[23]

The complete catalytic mechanism is summarized in Fig. 13. Initially, one XAN molecule enters the active site of XO and undergoes a nucleophilic attack by a hydroxyl group coordinated to Moco (Fig. 13 – 1). This attack is enhanced by Glu1261 when it abstracts the proton from the hydroxyl group. Then, a hydride is transferred from the previous tetrahedral intermediate to the sulfur atom coordinated to the Mo ion (Fig. 13 – 2). At this moment, the Mo ion is reduced from Mo(VI) to Mo(IV), and the URT molecule is formed. Finally, the Arg880 residue protonates the URT molecule triggering the release of the URC molecule from the active site to the solvent (Fig. 13 – 3).

At this stage, FAD is reduced to $FADH_2$, oxidizing Mo(IV) to its initial oxidation state of Mo(VI), promoting the deprotonation of the sulfur SO. This process is only possible due to two [2Fe–2S] clusters that establish a connection between Moco and FAD cofactors for the electron flow.

Afterward, a water molecule diffuses from a water tunnel settled between Glu1261 and Arg880 into the active site where it coordinates with the Mo ion (Fig. 13 – 4). Finally, the coordinated water molecule loses one proton to the solvent, and the enzymatic turnover is accomplished.

The description of the catalytic mechanism presented in this work provides new insights into the catalytic behavior of these types of enzymes, and the transition state structures can now be used to help in the development of transition state analogous inhibitors targeting XO.

Conflicts of interest

There are no conflicts of interest to declare.

Acknowledgements

This work was supported by the Applied Molecular Biosciences Unit – UCIBIO, which is financed by the national funds from FCT (UIDB/04378/2020), by the Associate Laboratory for Green Chemistry – LAQV, which is financed by the national funds from Fundacão para a Ciência e a Tecnologia, MCTES (FCT/MCTES; UIDB/50006/2020), and by the project PTDC/QUI-QFI/31689/2017. LBM wishes to thank FCT/MCTES for the CEEC-Individual 2017 Program Contract. HSF acknowledges FCT for his Ph.D. grant SFRH/BD/115396/2016.

Some of the calculations were produced with the support of INCD funded by FCT and FEDER under the project 01/SAICT/2016 number 022153.

The authors are also thankful to Prof. Maria João Ramos for granting access to QTREX, where some of the calculations were performed.

References

1 J. M. Pauff and R. Hille, Inhibition Studies of Bovine Xanthine Oxidase by Luteolin, Silibinin, Quercetin, and Curcumin, *J. Nat. Prod.*, 2009, **72**, 725–731.

2 D. Brule, G. Sarwar and L. Savoie, Changes in serum and urinary uric acid levels in normal human subjects fed purine-rich foods containing different amounts of adenine and hypoxanthine, *J. Am. Coll. Nutr.*, 1992, **11**, 353–358.

3 M. A. Becker, H. R. Schumacher Jr., R. L. Wortmann, P. A. MacDonald, D. Eustace, W. A. Palo, J. Streit and N. Joseph-Ridge, Febuxostat compared with allopurinol in patients with hyperuricemia and gout, *N. Engl. J. Med.*, 2005, **353**, 2450–2461.

4 M. A. Becker, H. R. Schumacher Jr., R. L. Wortmann, P. A. MacDonald, W. A. Palo, D. Eustace, L. Vernillet and N. Joseph-Ridge, Febuxostat, a novel nonpurine selective inhibitor of xanthine oxidase: a twenty-eight-day, multicenter, phase II, randomized, double-blind, placebo-controlled, dose-response clinical trial examining safety and efficacy in patients with gout, *Arthritis Rheum.*, 2005, **52**, 916–923.

5 H. R. Schumacher Jr., Febuxostat: a non-purine, selective inhibitor of xanthine oxidase for the management of hyperuricaemia in patients with gout, *Expert Opin. Invest. Drugs*, 2005, **14**, 893–903.

6 L. X. Chen and H. R. Schumacher, Gout: an evidence-based review, *J. Clin. Rheumatol.*, 2008, **14**, S55–S62.
7 P. Richette and T. Bardin, Gout, *Lancet*, 2010, **375**, 318–328.
8 N. Sakamoto, T. Yamamoto, Y. Moriwaki, T. Teranishi, M. Toyoda, Y. Onishi, S. Kuroda, K. Sakaguchi, T. Fujisawa, M. Maeda and T. Hada, Identification of a new point mutation in the human xanthine dehydrogenase gene responsible for a case of classical type I xanthinuria, *Hum. Genet.*, 2001, **108**, 279–283.
9 K. Ichida, Y. Amaya, N. Kamatani, T. Nishino, T. Hosoya and O. Sakai, Identification of two mutations in human xanthine dehydrogenase gene responsible for classical type I xanthinuria, *J. Clin. Invest.*, 1997, **99**, 2391–2397.
10 P. Pacher, A. Nivorozhkin and C. Szabo, Therapeutic effects of xanthine oxidase inhibitors: renaissance half a century after the discovery of allopurinol, *Pharmacol. Rev.*, 2006, **58**, 87–114.
11 R. V. Smalley, A. Guaspari, S. Haase-Statz, S. A. Anderson, D. Cederberg and J. A. Hohneker, Allopurinol: intravenous use for prevention and treatment of hyperuricemia, *J. Clin. Oncol.*, 2000, **18**, 1758–1763.
12 U. Kela and R. Vijayvargiya, Studies on the mechanism of action of 6-mercaptopurine. Interaction with copper and xanthine oxidase, *Biochem. J.*, 1981, **193**, 799–803.
13 Ö. Gunduğdu, S. A. A. Noma, T. Taskin-Tok, B. Ateş and N. Kishali, Evaluation of xanthine oxidase inhibitor properties on isoindoline-1,3-dion derivatives and calculation of interaction mechanism, *J. Mol. Struct.*, 2020, **1204**, 127523.
14 E. Huneycutt, C. Board and J. N. Clements, Lesinurad, a Selective URAT-1 Inhibitor With a Novel Mechanism in Combination With a Xanthine Oxidase Inhibitor, for Hyperuricemia Associated With Gout, *J. Pharm. Pract.*, 2018, **31**, 670–677.
15 A. Jordan and U. Gresser, Side Effects and Interactions of the Xanthine Oxidase Inhibitor Febuxostat, *Pharmaceuticals*, 2018, **11**(2), 51.
16 R. Kumar, G. Joshi, H. Kler, S. Kalra, M. Kaur and R. Arya, Toward an Understanding of Structural Insights of Xanthine and Aldehyde Oxidases: An Overview of their Inhibitors and Role in Various Diseases, *Med. Res. Rev.*, 2018, **38**, 1073–1125.
17 G. Luna, A. V. Dolzhenko and R. L. Mancera, Inhibitors of Xanthine Oxidase: Scaffold Diversity and Structure-Based Drug Design, *ChemMedChem*, 2019, **14**, 714–743.
18 N. Malik, P. Dhiman and A. Khatkar, In Silico and 3D QSAR Studies of Natural Based Derivatives as Xanthine Oxidase Inhibitors, *Curr. Top. Med. Chem.*, 2019, **19**, 123–138.
19 N. Masuoka and I. Kubo, Characterization of the xanthine oxidase inhibitory activity of alk(en)yl phenols and related compounds, *Phytochemistry*, 2018, **155**, 100–106.
20 A. Mehmood, M. Ishaq, L. Zhao, B. Safdar, A.-u. Rehman, M. Munir, A. Raza, M. Nadeem, W. Iqbal and C. Wang, Natural compounds with xanthine oxidase inhibitory activity: A review, *Chem. Biol. Drug Des.*, 2019, **93**, 387–418.
21 R. Ojha, J. Singh, A. Ojha, H. Singh, S. Sharma and K. Nepali, An updated patent review: xanthine oxidase inhibitors for the treatment of hyperuricemia and gout (2011–2015), *Expert Opin. Ther. Pat.*, 2017, **27**, 311–345.
22 C. Global, Burden of Disease Study, Global, regional, and national incidence, prevalence, and years lived with disability for 301 acute and chronic diseases and injuries in 188 countries, 1990–2013: a systematic analysis for the Global Burden of Disease Study 2013, *Lancet*, 2015, **386**, 743–800.
23 Y. Yamaguchi, T. Matsumura, K. Ichida, K. Okamoto and T. Nishino, Human Xanthine Oxidase Changes its Substrate Specificity to Aldehyde Oxidase Type upon Mutation of Amino Acid Residues in the Active Site: Roles of Active Site Residues in Binding and Activation of Purine Substrate, *J. Biochem.*, 2007, **141**, 513–524.
24 S. Metz and W. Thiel, A combined QM/MM study on the reductive half-reaction of xanthine oxidase: substrate orientation and mechanism, *J. Am. Chem. Soc.*, 2009, **131**, 14885–14902.
25 S. Metz and W. Thiel, QM/MM studies of xanthine oxidase: variations of cofactor, substrate, and active-site Glu802, *J. Phys. Chem. B*, 2010, **114**, 1506–1517.
26 K. Okamoto, Y. Kawaguchi, B. T. Eger, E. F. Pai and T. Nishino, Crystal Structures of Urate Bound Form of Xanthine Oxidoreductase: Substrate Orientation and Structure of the Key Reaction Intermediate, *J. Am. Chem. Soc.*, 2010, **132**, 17080–17083.
27 Y. Yamaguchi, T. Matsumura, K. Ichida, K. Okamoto and T. Nishino, Human xanthine oxidase changes its substrate specificity to aldehyde oxidase type upon mutation of amino acid residues in the active site: roles of active site residues in binding and activation of purine substrate, *J. Biochem.*, 2007, **141**, 513–524.
28 A. R. Pearson, B.L.J. Godber, R. Eisenthal, G.L. Taylor and R. Harrison, *Human Milk Xanthine Dehydrogenase is Incompletely Converted to the Oxidase Form in the Absence of Proteolysis. A Structural Explanation*, 2006, DOI: 10.2210/pdb2ckj/pdb.
29 S. F. Altschul, T. L. Madden, A. A. Schaffer, J. Zhang, Z. Zhang, W. Miller and D. J. Lipman, Gapped BLAST and PSI-BLAST: a new generation of protein database search programs, *Nucleic Acids Res.*, 1997, **25**, 3389–3402.
30 S. F. Altschul, J. C. Wootton, E. M. Gertz, R. Agarwala, A. Morgulis, A. A. Schaffer and Y. K. Yu, Protein database searches using compositionally adjusted substitution matrices, *FEBS J.*, 2005, **272**, 5101–5109.
31 N. Guex, M. C. Peitsch and T. Schwede, Automated comparative protein structure modeling with SWISS-MODEL and Swiss-PdbViewer: a historical perspective, *Electrophoresis*, 2009, **30**(Suppl 1), S162–S173.
32 P. Benkert, M. Biasini and T. Schwede, Toward the estimation of the absolute quality of individual protein structure models, *Bioinformatics*, 2011, **27**, 343–350.
33 S. Bienert, A. Waterhouse, T. A. de Beer, G. Tauriello, G. Studer, L. Bordoli and T. Schwede, The SWISS-MODEL

Repository-new features and functionality, *Nucleic Acids Res.*, 2017, **45**, D313–D319.

34 A. Waterhouse, M. Bertoni, S. Bienert, G. Studer, G. Tauriello, R. Gumienny, F. T. Heer, T. A. P. de Beer, C. Rempfer, L. Bordoli, R. Lepore and T. Schwede, SWISS-MODEL: homology modelling of protein structures and complexes, *Nucleic Acids Res.*, 2018, **46**, W296–W303.

35 J. Wang, R. M. Wolf, J. W. Caldwell, P. A. Kollman and D. A. Case, Development and testing of a general amber force field, *J. Comput. Chem.*, 2004, **25**, 1157–1174.

36 V. Hornak, R. Abel, A. Okur, B. Strockbine, A. Roitberg and C. Simmerling, Comparison of multiple Amber force fields and development of improved protein backbone parameters, *Proteins*, 2006, **65**, 712–725.

37 P. Ferreira, N. Cerqueira, N. F. Bras, P. A. Fernandes and M. J. Ramos, Parametrization of Molybdenum Cofactors for the AMBER Force Field, *J. Chem. Theory Comput.*, 2018, **14**, 2538–2548.

38 D. A. Case, T. A. Darden, T. E. Cheatham, C. L. Simmerling, J. Wang, R. E. Duke, R. Luo, R. C. Walker, W. Zhang, K. M. Merz, B. Roberts, S. Hayik, A. Roitberg, G. Seabra, J. Swails, A. W. Goetz, I. Kolossváry, K. F. Wong, F. Paesani, J. Vanicek, R. M. Wolf, J. Liu, X. Wu, S. R. Brozell, T. Steinbrecher, H. Gohlke, Q. Cai, X. Ye, J. Wang, M. J. Hsieh, G. Cui, D. R. Roe, D. H. Mathews, M. G. Seetin, R. Salomon-Ferrer, C. Sagui, V. Babin, T. Luchko, S. Gusarov, A. Kovalenko and P. A. Kollman, *AMBER 12*, 2012, DOI: citeulike-article-id:10779586.

39 M. H. Olsson, C. R. Sondergaard, M. Rostkowski and J. H. Jensen, PROPKA3: Consistent Treatment of Internal and Surface Residues in Empirical pKa Predictions, *J. Chem. Theory Comput.*, 2011, **7**, 525–537.

40 C. R. Søndergaard, M. H. M. Olsson, M. Rostkowski and J. H. Jensen, Improved Treatment of Ligands and Coupling Effects in Empirical Calculation and Rationalization of pKa Values, *J. Chem. Theory Comput.*, 2011, **7**, 2284–2295.

41 D. J. Price and C. L. Brooks III, A modified TIP3P water potential for simulation with Ewald summation, *J. Chem. Phys.*, 2004, **121**, 10096–10103.

42 R. Zwanzig, Nonlinear generalized Langevin equations, *J. Stat. Phys.*, 1973, **9**, 215–220.

43 H. J. C. Berendsen, J. P. M. Postma, W. F. v. Gunsteren, A. DiNola and J. R. Haak, Molecular dynamics with coupling to an external bath, *J. Chem. Phys.*, 1984, **81**, 3684–3690.

44 N. M. F. S. A. Cerqueira, P. A. Fernandes and M. J. Ramos, Protocol for Computational Enzymatic Reactivity Based on Geometry Optimisation, *ChemPhysChem*, 2018, **19**, 669–689.

45 H. S. Fernandes, M. J. Ramos and N. M. F. S. A. Cerqueira, molUP: A VMD plugin to handle QM and ONIOM calculations using the gaussian software, *J. Comput. Chem.*, 2018, **39**, 1344–1353.

46 W. Humphrey, A. Dalke and K. Schulten, VMD: visual molecular dynamics, *J. Mol. Graphics*, 1996, **14**, 33–38, 27–38.

47 F. Maseras and K. Morokuma, IMOMM: A new integrated ab initio + molecular mechanics geometry optimization scheme of equilibrium structures and transition states, *J. Comput. Chem.*, 1995, **16**, 1170–1179.

48 M. Svensson, S. Humbel, R. D. J. Froese, T. Matsubara, S. Sieber and K. Morokuma, ONIOM: A Multilayered Integrated MO + MM Method for Geometry Optimizations and Single Point Energy Predictions. A Test for Diels–Alder Reactions and Pt(P(t-Bu)3)2 + H2 Oxidative Addition, *J. Phys. Chem.*, 1996, **100**, 19357–19363.

49 S. Dapprich, I. Komaromi, K. S. Byun, K. Morokuma and M. J. Frisch, A new ONIOM implementation in Gaussian98. Part I. The calculation of energies, gradients, vibrational frequencies and electric field derivatives, *J. Mol. Struct.: THEOCHEM*, 1999, **461**, 1–21.

50 T. Yanai, D. P. Tew and N. C. Handy, A new hybrid exchange-correlation functional using the Coulomb-attenuating method (CAM-B3LYP), *Chem. Phys. Lett.*, 2004, **393**, 51–57.

51 R. Ditchfield, W. J. Hehre and J. A. Pople, Self-Consistent Molecular-Orbital Methods. IX. An Extended Gaussian-Type Basis for Molecular-Orbital Studies of Organic Molecules, *J. Chem. Phys.*, 1971, **54**, 724–728.

52 W. J. Hehre, R. Ditchfield and J. A. Pople, Self-Consistent Molecular Orbital Methods. XII. Further Extensions of Gaussian-Type Basis Sets for Use in Molecular Orbital Studies of Organic Molecules, *J. Chem. Phys.*, 1972, **56**, 2257–2261.

53 P. C. Hariharan and J. A. Pople, The influence of polarization functions on molecular orbital hydrogenation energies, *Theor. Chim. Acta*, 1973, **28**, 213–222.

54 M. M. Francl, W. J. Pietro, W. J. Hehre, J. S. Binkley, M. S. Gordon, D. J. DeFrees and J. A. Pople, Self-consistent molecular orbital methods. XXIII. A polarization-type basis set for second-row elements, *J. Chem. Phys.*, 1982, **77**, 3654–3665.

55 M. S. Gordon, J. S. Binkley, J. A. Pople, W. J. Pietro and W. J. Hehre, Self-consistent molecular-orbital methods. 22. Small split-valence basis sets for second-row elements, *J. Am. Chem. Soc.*, 1982, **104**, 2797–2803.

56 P. J. Hay and W. R. Wadt, Ab initio effective core potentials for molecular calculations. Potentials for K to Au including the outermost core orbitals, *J. Chem. Phys.*, 1985, **82**, 299–310.

57 M. J. Frisch, G. W. Trucks, H. B. Schlegel, G. E. Scuseria, M. A. Robb, J. R. Cheeseman, G. Scalmani, V. Barone, B. Mennucci, G. A. Petersson, H. Nakatsuji, M. Caricato, X. Li, H. P. Hratchian, A. F. Izmaylov, J. Bloino, G. Zheng, J. L. Sonnenberg, M. Hada, M. Ehara, K. Toyota, R. Fukuda, J. Hasegawa, M. Ishida, T. Nakajima, Y. Honda, O. Kitao, H. Nakai, T. Vreven, J. A. Montgomery Jr., J. E. Peralta, F. Ogliaro, M. J. Bearpark, J. Heyd, E. N. Brothers, K. N. Kudin, V. N. Staroverov, R. Kobayashi, J. Normand, K. Raghavachari, A. P. Rendell, J. C. Burant, S. S. Iyengar, J. Tomasi, M. Cossi, N. Rega, N. J. Millam, M. Klene, J. E. Knox, J. B. Cross, V. Bakken, C. Adamo, J. Jaramillo,

R. Gomperts, R. E. Stratmann, O. Yazyev, A. J. Austin, R. Cammi, C. Pomelli, J. W. Ochterski, R. L. Martin, K. Morokuma, V. G. Zakrzewski, G. A. Voth, P. Salvador, J. J. Dannenberg, S. Dapprich, A. D. Daniels, Ö. Farkas, J. B. Foresman, J. V. Ortiz, J. Cioslowski and D. J. Fox, *Gaussian 09*, 2009.

58 R. Krishnan, J. S. Binkley, R. Seeger and J. A. Pople, Self-consistent molecular orbital methods. XX. A basis set for correlated wave functions, *J. Chem. Phys.*, 1980, **72**, 650–654.

59 A. D. McLean and G. S. Chandler, Contracted Gaussian basis sets for molecular calculations. I. Second row atoms, Z=11–18, *J. Chem. Phys.*, 1980, **72**, 5639–5648.

60 T. Clark, J. Chandrasekhar, G. W. Spitznagel and P. V. R. Schleyer, Efficient diffuse function-augmented basis sets for anion calculations. III. The 3–21+G basis set for first-row elements, Li-F, *J. Comput. Chem.*, 1983, **4**, 294–301.

61 M. J. Frisch, J. A. Pople and J. S. Binkley, Self-consistent molecular orbital methods 25. Supplementary functions for Gaussian basis sets, *J. Chem. Phys.*, 1984, **80**, 3265–3269.

62 G. W. Spitznagel, T. Clark, P. v. R. Schleyer and W. J. Hehre, An evaluation of the performance of diffuse function-augmented basis sets for second row elements, Na-Cl, *J. Comput. Chem.*, 1987, **8**, 1109–1116.

63 H. S. Fernandes, S. F. Sousa and N. M. F. S. A. Cerqueira, VMD Store–A VMD Plugin to Browse, Discover, and Install VMD Extensions, *J. Chem. Inf. Model.*, 2019, **59**(11), 4519–4523.

64 R. P. Magalhães, H. S. Fernandes and S. F. Sousa, Modelling Enzymatic Mechanisms with QM/MM Approaches: Current Status and Future Challenges, *Isr. J. Chem.*, 2020, **60**, 655.

65 S. F. Sousa, A. J. M. Ribeiro, R. P. P. Neves, N. F. Brás, N. M. F. S. A. Cerqueira, P. A. Fernandes and M. J. Ramos, Application of quantum mechanics/molecular mechanics methods in the study of enzymatic reaction mechanisms, *Wiley Interdiscip. Rev.: Comput. Mol. Sci.*, 2017, **7**, e1281.

66 H. S. Fernandes, M. J. Ramos and N. Cerqueira, The Catalytic Mechanism of the Pyridoxal-5′-phosphate-Dependent Enzyme, Histidine Decarboxylase: A Computational Study, *Chemistry*, 2017, **23**, 9162–9173.

67 H. S. Fernandes, M. J. Ramos and N. M. F. S. A. Cerqueira, Catalytic Mechanism of the Serine Hydroxymethyltransferase: A Computational ONIOM QM/MM Study, *ACS Catal.*, 2018, 10096–10110, DOI: 10.1021/acscatal.8b02321.

68 C. S. S. Teixeira, M. J. Ramos, S. F. Sousa and N. M. F. S. A. Cerqueira, Solving the Catalytic Mechanism of Tryptophan Synthase: an Emergent Drug Target in the Treatment of Tuberculosis, *ChemCatChem*, 2020, **12**, 227–237.

69 S. Sudhakara, C. Ramakrishnan, M. M. Gromiha and A. Chadha, New insights into the stereospecific reduction by an (S) specific carbonyl reductase from Candida parapsilosis ATCC 7330: experimental and QM/MM studies, *Catal. Sci. Technol.*, 2020, **10**, 5925–5934.

70 W.-S. Ren, K.-B. Jiang, H. Deng, N. Lu, T. Yu, H. Guo and P. Qian, Catalytic Mechanism and Product Specificity of Protein Arginine Methyltransferase PRMT7: A Study from QM/MM Molecular Dynamics and Free Energy Simulations, *J. Chem. Theory Comput.*, 2020, **16**, 5301–5312.

71 J. Bai, L. Yan and Y. Liu, Catalytic mechanism of the PrhA (V150L/A232S) double mutant involved in the fungal meroterpenoid biosynthetic pathway: a QM/MM study, *Phys. Chem. Chem. Phys.*, 2019, **21**, 25658–25668.

72 J. McClory, C. Hui, J. Zhang and M. Huang, The phosphorylation mechanism of mevalonate diphosphate decarboxylase: a QM/MM study, *Org. Biomol. Chem.*, 2020, **18**, 518–529.

73 Y. Yu, X. Wang, Y. Gao, Y. Yang, L. Sun, G. Wang, X. Deng and X. Niu, Molecular modeling and QM/MM calculation clarify the catalytic mechanism of β-lactamase N1, *J. Mol. Model.*, 2019, **25**, 118.

74 N. M. F. S. A. Cerqueira, P. J. Gonzalez, P. A. Fernandes, J. J. G. Moura and M. J. Ramos, Periplasmic Nitrate Reductase and Formate Dehydrogenase: Similar Molecular Architectures with Very Different Enzymatic Activities, *Acc. Chem. Res.*, 2015, **48**, 2875–2884.

75 N. M. F. S. A. Cerqueira, P. J. Gonzalez, C. D. Brondino, M. J. Romão, C. C. Romão, I. Moura and J. J. G. Moura, The effect of the sixth sulfur ligand in the catalytic mechanism of periplasmic nitrate reductase, *J. Comput. Chem.*, 2009, **30**, 2466–2484.

76 N. M. F. S. A. Cerqueira, P. A. Fernandes, P. J. Gonzalez, J. J. G. Moura and M. J. Ramos, The Sulfur Shift: An Activation Mechanism for Periplasmic Nitrate Reductase and Formate Dehydrogenase, *Inorg. Chem.*, 2013, **52**, 10766–10772.

77 O. Caldararu, M. Feldt, D. Cioloboc, M.-C. van Severen, K. Starke, R. A. Mata, E. Nordlander and U. Ryde, QM/MM study of the reaction mechanism of sulfite oxidase, *Sci. Rep.*, 2018, **8**, 4684.

78 G. Dong and U. Ryde, Reaction mechanism of formate dehydrogenase studied by computational methods, *JBIC, J. Biol. Inorg. Chem.*, 2018, **23**, 1243–1254.

79 L. B. Maia and J. J. G. Moura, Putting xanthine oxidoreductase and aldehyde oxidase on the NO metabolism map: Nitrite reduction by molybdoenzymes, *Redox Biol.*, 2018, **19**, 274–289.

80 R. Hille, The Mononuclear Molybdenum Enzymes, *Chem. Rev.*, 1996, **96**, 2757–2816.

81 P. Ferreira, N. M. F. S. A. Cerqueira, P. A. Fernandes, M. J. Romão and M. J. Ramos, Catalytic Mechanism of Human Aldehyde Oxidase, *ACS Catal.*, 2020, **10**, 9276–9286.

